

# The 23 January 2014 Jizan earthquake and its tectonic implications in southwestern Saudi Arabia



A.K. Abdelfattah<sup>a,b,\*</sup>, A. Al-Amri<sup>a</sup>, A.K. Abd el-aal<sup>b</sup>, Faisal K. Zaidi<sup>a</sup>, M. Fnais<sup>a,c</sup>, S. Almadani<sup>a</sup>, N. Al-Arifi<sup>a</sup>

<sup>a</sup> Department of Geology & Geophysics, King Saud University, Riyadh 11451, Saudi Arabia

<sup>b</sup> National Research Institute of Astronomy and Geophysics, 11421 Helwan, Cairo, Egypt

<sup>c</sup> Princess Nourah bint Abdulrahman University, Riyadh, Saudi Arabia

## ARTICLE INFO

### Article history:

Received 18 September 2016

Received in revised form 25 May 2017

Accepted 29 May 2017

Available online 31 May 2017

### Keywords:

Hypocenter locations

Focal mechanism solutions

Seismogenic stress domain

Saudi Arabia

## ABSTRACT

A moderate-sized earthquake of Mw 4.4 occurred in southwestern Saudi Arabia on 23 January 2014. The event is considered as the largest observed earthquake that has occurred in the epicentral area. To examine the seismogenic stress regime and resolve the fault plane ambiguity, the hypocenter locations and focal mechanisms were determined using well recorded waveforms of the broadband stations operated by the Saudi Geological Survey. The current analysis included dataset consisting of mainshock and a total number of 113 well-located aftershocks. Focal mechanism solutions of the mainshock and fifteen aftershocks were determined. The focal mechanism solutions were inverted using stress tensor inversion. It indicates that the maximum compressive stress,  $\sigma_1$ , has a nearly shallow plunge ( $11.8^\circ$ ) of ESE orientation and minimum compressive stress,  $\sigma_3$ , has a shallow plunge ( $0.3^\circ$ ) toward NNE. Our results obtained from precise earthquake locations, focal mechanism solutions and stress tensor inversion reveal dextral strike-slip faulting over the ENE-WSW striking plane. The analysis of Coulomb failure stress emphasized the causative fault of the 2014 Jizan earthquake sequence. The active fault implies a reactivation of a high-angle fault, buried in the Precambrian basement, which is conjugate to the Red Sea spreading axis and NNW-SSE Najd fault system. The present study provided an impetus toward understanding the seismogenic stress regime in a virgin area.

© 2017 Elsevier B.V. All rights reserved.

## 1. Introduction

Kinematic plate motions revealed that the extensional stress regime acting on the Africa-Arabia plate boundary in the Red Sea is the dominant stress responsible for the seismic activities occurring in the region (Bonatti, 1985; Girdler and Underwood, 1985; McClusky et al., 2010). The Arabian Shield has experienced historical and instrumental earthquakes. The recent earthquakes include those of Tabuk in 2004 (Mw 5.1); Badr in 2009 (Mw 3.7); and Harrat Lunayyir in 2009 (Mw 5.7) which originated in a volcanic field due to dike intrusion. These earthquakes occurred in the upper crust of the Arabian Shield at focal depths of 10 km. Focal mechanisms of these earthquakes display normal faults of NW-SE orientations, parallel to the Red Sea rift axis, due to the EW extensional and NS compression stress domain in the Arabian Shield. This is thought to be imparted from the ambient stress regime associated with the Red Sea rifting system (Aldamegh et al., 2009; Craig et al., 2011; Abdel-Fattah et al., 2014; Aldamegh et al., 2012). This stress system reactivated the Precambrian basement faults several times during the

geological history of the region (Agar, 1992; Hussein, 1988; Stern and Johnson, 2010).

A moderate-sized earthquake with ML 4.5 occurred in the southern part of the Arabian Shield in Jizan area on the 23rd of January 2014. It is noteworthy that no instruments were present in the epicentral area before the installation of the Saudi Seismic Network in 2012. The mainshock of a maximum modified Mercalli intensity of V to VI was widely felt in the epicentral area (El-Hadidy, 2015). The waveform data set of the 2014 Jizan earthquake, which was recorded by the broadband stations operated by the Saudi Geological Survey (SGS), provided an impetus toward investigating the seismotectonic implications. In this study we determined precise hypocenter locations and focal mechanism solutions, stress tensor inversion and Coulomb failure stress. The analysis might help to resolve the causative fault plane of the 2014 Jizan earthquake sequence and then to compile the results in the perspective of regional tectonic implications of the Red Sea rifting system and the Gulf of Aden.

## 2. Geological and tectonic settings

The Arabian shield exposed in the Western part of Saudi Arabia consists mainly of basement rocks ranging in age from 1000 million years to 545 million years. This Precambrian basement formed the base of a thick

\* Corresponding author at: Department of Geology & Geophysics, College of Science, King Saud University, Riyadh 11451, Saudi Arabia.

E-mail address: [ali\\_kamel100@yahoo.co.uk](mailto:ali_kamel100@yahoo.co.uk) (A.K. Abdelfattah).

sequence of late Oligocene to Holocene volcanic rocks developed within the framework of the Red sea opening and spreading (Camp and Roobol, 1989). Geologically, the epicentral area is a part of the Arabian Shield (Fig. 1) and comprises mainly of the Proterozoic igneous and metamorphosed igneous rocks. The Palaeozoic and Mesozoic Era are represented by the Wajid sandstone, Khums Formation and the Hanifa Formation. The Cenozoic Era is dominated by the presence of the undifferentiated quaternary sediments which occupy the coastal zone and form a part of the Tihama coastal plains. The region has experienced a number of

volcanic activities during the Neogene to Quaternary period. Quaternary basalts in the region notarize the appearance of magmatic activity associated with the rifting process.

The area has been subjected to tectonic activity with the major structural movements taking place in the Tertiary period due to rifting associated with the present-day tectonics of the Red Sea and the Gulf of Aden (Coleman, 1977; Coleman et al., 1977). The seismic activity in this region is tectonically attributed to the complex triple junction of active spreading ridges along the Red Sea, Gulf of Aden and East African Rift Zone,

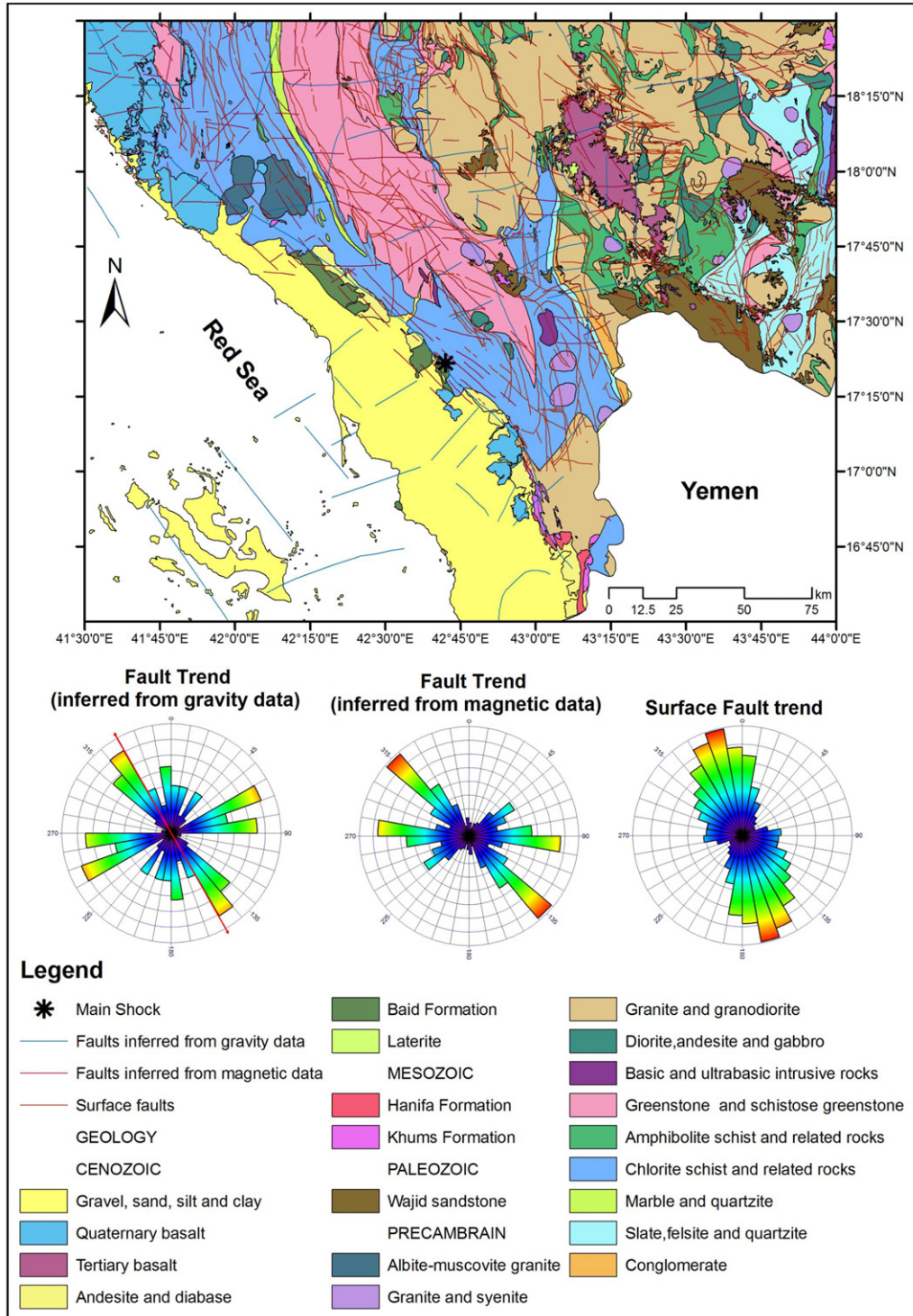


Fig. 1. Map showing geological settings, surface and subsurface fault trends in the region of the epicentre area. (Modified from the digital geological map of Saudi Arabia prepared by SGS)

respectively. Spreading rates of Red Sea vary between  $<10$  mm/year to  $\sim 16$  mm/year (Chu and Gordon, 1998) thus designating the Red Sea rift as an ultra-slow spreading rift (Augustin et al., 2016; Carbotte et al., 2015; Dick et al., 2003). GPS records reveals that the geodetic Euler vector of Arabia relative to Nubia is  $31.7^\circ\text{N}$ ,  $24.6^\circ\text{E}$ , with anticlockwise rotation of  $0.37^\circ\text{Myr}^{-1}$  (Reilinger et al., 2006; ArRajehi et al., 2010). This suggests that the rate of Red Sea spreading is greater in the south than in the north. This is evident from the width of the Red Sea which is about 200 km in the north at latitude  $27^\circ\text{N}$  and 350 km in the south at latitude  $17^\circ\text{N}$  (Rasul et al., 2015). Historical and recent earthquakes have occurred in the southern Red Sea and southwestern Saudi Arabia. Tectonically, three types of faults of normal to strike-slip displacements dominate in the area. The faults are the NW–SE Red Sea rift system, NNW–SSE Najd Fault system (NFS) of sinistral strike-slip movement, and the conjugated faults of dextral strike-slip displacement striking in an ENE–WSW direction; representing the Precambrian Pan-African structures (Johnson, 1998; Vita-Finzi, 2001; Fournier et al., 2007). The prominent faults in the study area and their trend have been shown in Fig. 1 and include surface faults and faults inferred from gravity and magnetic data (Gettings, 1983). The prominent surface fault direction is N15 W corresponding to the red sea rift axis). The mean direction of faults inferred from gravity data is N30 W, but three prominent fault trends can be seen; NNW–SSE, NW–SE and NE–SW. Faults inferred from magnetic data show two prominent directions i.e. NW–SE and WNW–ESE. A third set trending in direction of the red sea transform fault system (NE–SW) is also seen.

Over all the Tertiary tectonic is represented mainly by the NNW trending fault system as is visible in the rose diagrams in Fig. 1. However faults trending in the direction of the Najd fault system and faults trending in the direction of the transform faults related to the Red sea rifting process are also present in the area. Although a number of earthquakes occurred in the southwestern of Saudi Arabia, there is no focal mechanism catalogue available for the region.

The spatial distribution of seismicity in the epicentral area and its vicinity is shown in Fig. 2, for earthquake catalogue compiled by Saudi Geological Survey (SGS) from 2007 to 2014. It is obvious from Fig. 2 that the seismicity in the region appears as scattered clusters and shows no relative fault trends.

### 3. Locations and focal mechanisms

The mainshock location and the broadband seismic stations which recorded the 2014 Jizan earthquake are shown in Fig. 2. These stations are equipped with Trillium velocity seismometers of three-component having a response spectrum in the period range of 0.02–40 and 0.02–120 s and digitized by 24-bit A/D at sampling rate of 50 Hz. The waveform dataset was visually examined to remove the recordings characterized by low signal-to-noise ratio, missed recordings and overlapping of successive events. Based on the above criteria, we analyzed the mainshock and 113 aftershocks within the period between January 2014 and December 2014.

#### 3.1. Hypocentre locations

Hypocenters were determined using the ELOCATE code of Herrmann and Ammon (2004). We followed an algorithm similar to the master event method. We first selected the mainshock, as a reference event, that displayed clear P and S waves to provide the high accuracy picking of the arrival times. The arrival times of P waves were picked from vertical component recordings while the two horizontal components are used for S waves using GSAC software program. The differential arrival times between secondary events and the reference event were measured using the cross-correlation technique with time shifts of 0.001 s only for events giving a normalized correlation coefficient higher than 0.8 within the frequency range 1–6 Hz. Following this algorithm, the accuracy of arrival times is relatively improved to be about 10 ms. A priori information weights were given for P and S waves, respectively. The theoretical arrival times of P and S waves were calculated using the velocity model of Rodgers et al. (1999) beneath the Arabian Shield; listed in Table 1. The algorithm was effective for events with similar waveforms. The results reflected averaged root mean squares (RMS) of 0.08 for P wave and 0.12 for S wave. The errors in location were within 0.67 km horizontally and 0.91 km in depth.

The seismic activity of the 23rd of January 2014 Jizan earthquake sequence is characterized by mainshock-aftershocks pattern. We located a total number of 113 aftershocks in the magnitude range of 0.5–3.8. The mainshock was followed by only three events of magnitude  $>3.0$ , 12

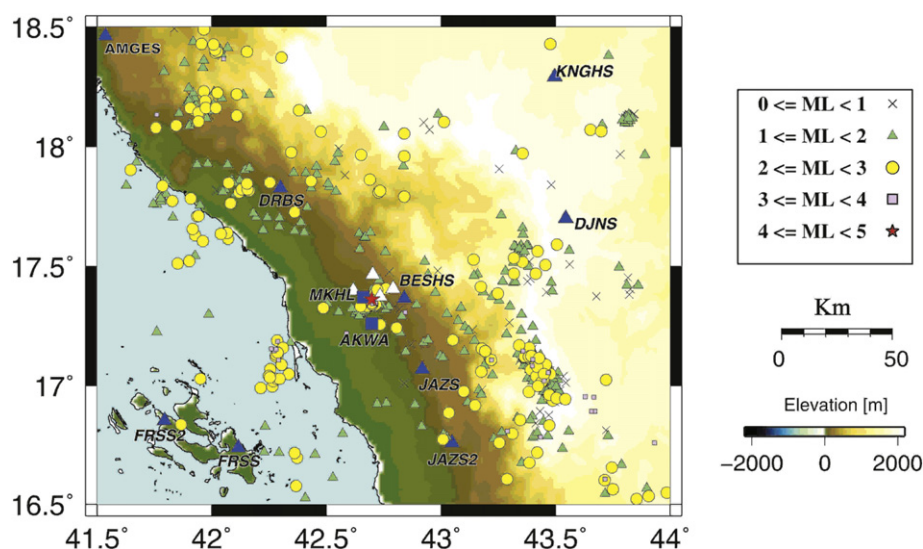


**Fig. 2.** Map showing seismicity in the region (2007–2014) as compiled by SGS. The main shock that occurred on 23 January 2014 is represented by red star. The map also shows the distribution of seismic stations used for the hypocenter location and focal mechanism solution. Blue triangles show the permanent seismic stations where as the temporal seismic stations, installed between 5 February 2014 to 23 June 2014, are shown by white triangles. Blue squares represent two permanent seismic stations, AKWA and MKHL, installed on 5 February 2014. The stations AKWA and MKHL are to the west of the mainshock. (For interpretation of the references to colour in this figure legend, the reader is referred to the web version of this article.)

**Table 1**

One dimensional velocity model beneath the Arabian Shield as deduced by Rodgers et al. (1999) for P- and S-wave velocities used for calculation of the Green's functions.

H [km]	V <sub>P</sub> [km/s]	V <sub>S</sub> [km/s]
01	4.0	2.31
15	6.2	3.58
20	6.8	3.93
–	7.9	4.30

H layer thickness, VP P-wave velocity, and VS S-wave velocity.

aftershocks of magnitudes  $2.0 < M_L < 3.0$ , and 98 aftershocks in the magnitude range of 0.5–2.0. The hypocentral parameters are listed in Table 2. The spatial distribution of epicentres with magnitude classification is illustrated in Fig. 3. In addition, the figure shows the vertical cross-sections of hypocentre distribution parallel to the latitude and longitude. It is noteworthy that the majority of aftershock distributions delineated the source volume of the respective sequence; providing a rough estimate of the potential size of the mainshock dimensions of 6 km fault length, 2 km width and 10 km down-dip extent.

### 3.2. Focal mechanism solutions

To understand the tectonic processes causing localized seismic deformation, focal mechanism solutions are required. In the present study, two methods were used to retrieve the focal mechanism solutions. The first method is the moment tensor inversion technique of Yagi and Nishimura (2011) that depended on using waveforms recorded by the broadband stations. Due to low signal to noise ratio in the low frequency band, focal mechanisms were retrieved using moment tensor inversion for the mainshock only. The technique is used to analyze the long period seismic waves in the frequency range of 0.01–0.1 Hz, which are relatively insensitive to the complex effects of source finiteness and propagation heterogeneities (Ritsema and Lay, 1995; Plicka and Zahradnik, 2014). Waveforms were instrumentally corrected to the ground displacement and filtered by a second order band pass filter in the frequency range of 0.01–0.1 Hz to be compatible with the point-source assumption that becomes validated when the wavelengths are much larger than the source dimensions. Since we used waveform of long period characteristics, the sampling rate of 1 Hz and a generic velocity model was used to compute the Green's functions depending on the discrete wave number method of Kohketsu (1985). The crustal model of the Arabian shield deduced by Rodgers et al. (1999), Table 1, was used to estimate the Green's functions. The quality factor  $Q$  are assigned according to Swanger's law " $Q_s = V_s/10$ ", where  $V_s$  is the shear velocity in meter per second and  $Q_P \approx 9/4Q_s$  (Mancilla, 2001). During the moment tensor inversion course, the damped least squares were iterated over a set of focal depths

in the range of 2–20 km. The results showed an optimum focal mechanism solution at focal depth of 10 km. Fig. 4 shows the moment tensor solution of the mainshock and the corresponding synthetic seismograms compared with the observed ones. The extracted moment tensor was decomposed into the percentages of 0.0% ISO, 68.9% DC, and 31.1% CLVD according to Vavryčuk (2015).

For fourteen aftershocks of  $M_L$  larger than 2, as determined by SGS, the method of Zahradnik et al. (2001) was used to retrieve the focal mechanism solution, focal depth, and moment magnitude. The technique is based on modelling the spectral amplitudes constraint with the first motion polarities of P wave; assuming a double-coupled point source. The discrete wave number method of Bouchon (1981) and Coutant (1989) is used to calculate synthetic Green functions, while take-off angles are calculated using the ray-method code ANGGRA (Jansky, 2001) for the first-motion polarities that were carefully picked from seismograms. The waveforms were instrumentally corrected to ground velocity, a second-order Butterworth band-pass filter with corners at 1.0 and 2.0 Hz was applied to the waveform data, and thus the amplitude spectrum was calculated by the FFT algorithm. The best-fit double-couple solution was determined using a grid search over the space parameters (strike, dip, and rake) with an interval of 2°. Moreover, the focal depth was assessed over a series of Green's functions in the depth range of 2–20 km with an increment of 2 km. For the analyzed aftershocks, the moment magnitude that corresponded to the estimated seismic moment ranged from 1.6 to 3.4 based on Hanks and Kanamori (1979).

Focal mechanism solutions for 15 earthquakes of the sequence are shown in Fig. 5 and their focal parameters are listed in Table 2. It is noteworthy that the sequence mainly occurred on a strike-slip fault combined with a slight dip-slip displacement. The precise hypocenter locations and focal mechanism solutions have delineated the causative fault of the 2014 Jizan earthquake sequence. The distribution of epicentres, as shown in Fig. 3, is aligned in the ENE-WSW direction, constrained by the fault orientation of strike N260.5°E that is conjugate to the NW to NNW active faults in Arabian Shield. The aftershocks mostly generated west of the mainshock epicentre; reflecting a probable localized stress distribution zone. The focal mechanisms, Fig. 5, displayed dextral strike-slip with slight dip-slip displacements. The result strongly suggested that a steep angle fault buried in the Precambrian basement was reactivated along the ENE-WSW trend.

### 4. Stress inversion

The focal mechanisms provided an impetus toward investigating the seismogenic stress. For this purpose, we use the code of Vavryčuk (2014), hereafter STRESSINVERSE. The method depends on an iterative technique to determine the values of principal stress directions and the

**Table 2**

Hypocentral and fault plane parameters of the analyzed events with  $M_L$  larger than 2, as determined by Saudi Geological Survey.

Date	O.T.	Lat. [°]	Long. [°]	Depth	ERH	ERZ	Mo [Nm]	Mw	Fault parameters			ID
									Strike	Dip	Rake	
20140123	150,036.59	17.3493	42.6977	10	0.12	0.29	5.21E+15	4.4	259 ± 2	87 ± 2	–171 ± 4	Mainshock
20140123	214,622.24	17.3422	42.6777	08	0.27	0.36	1.12E+12	2.0	260 ± 11	79 ± 7	–150 ± 16	F1
20140123	215,018.17	17.3508	42.6885	10	0.39	0.47	7.60E+11	1.9	260 ± 10	78 ± 6	–156 ± 18	F2
20140124	120,222.36	17.3484	42.7143	11	0.41	0.54	6.87E+11	1.8	255 ± 16	88 ± 5	–160 ± 11	F3
20140124	120,640.62	17.3432	42.6768	09	0.32	0.43	1.22E+12	2.0	242 ± 9	84 ± 2	–175 ± 10	F4
20140125	002813.04	17.3433	42.6817	13	0.18	0.32	8.52E+13	3.3	251 ± 5	78 ± 2	–164 ± 12	F5
20140125	020911.12	17.3465	42.6698	08	0.37	0.44	1.11E+12	2.0	248 ± 10	77 ± 4	–167 ± 13	F6
20140126	122,626.73	17.3467	42.6673	08	0.21	0.17	4.37E+13	3.1	257 ± 3	75 ± 2	–156 ± 7	F7
20140204	014952.45	17.3428	42.6753	12	0.28	0.30	1.21E+12	2.0	247 ± 12	87 ± 1	–172 ± 1	F8
20140204	015213.51	17.3418	42.6812	11	0.45	0.63	4.92E+11	1.7	248 ± 15	84 ± 3	–163 ± 9	F9
20140715	190,817.03	17.3458	42.7011	08	0.22	0.28	1.18E+12	2.0	250 ± 8	78 ± 8	164 ± 6	F10
20140803	202,111.28	17.3482	42.6857	08	0.15	0.18	1.24E+14	3.4	247 ± 3	80 ± 2	153 ± 7	F11
20140803	202,629.02	17.3448	42.6997	10	0.29	0.46	3.57E+11	1.6	245 ± 19	78 ± 8	–167 ± 3	F12
20140804	060443.04	17.3522	42.7212	08	0.21	0.31	1.98E+12	2.1	246 ± 11	70 ± 5	–174 ± 4	F13
20140817	032705.26	17.3447	42.6982	08	0.20	0.24	3.46E+12	2.3	245 ± 2	82 ± 2	–143 ± 19	F14

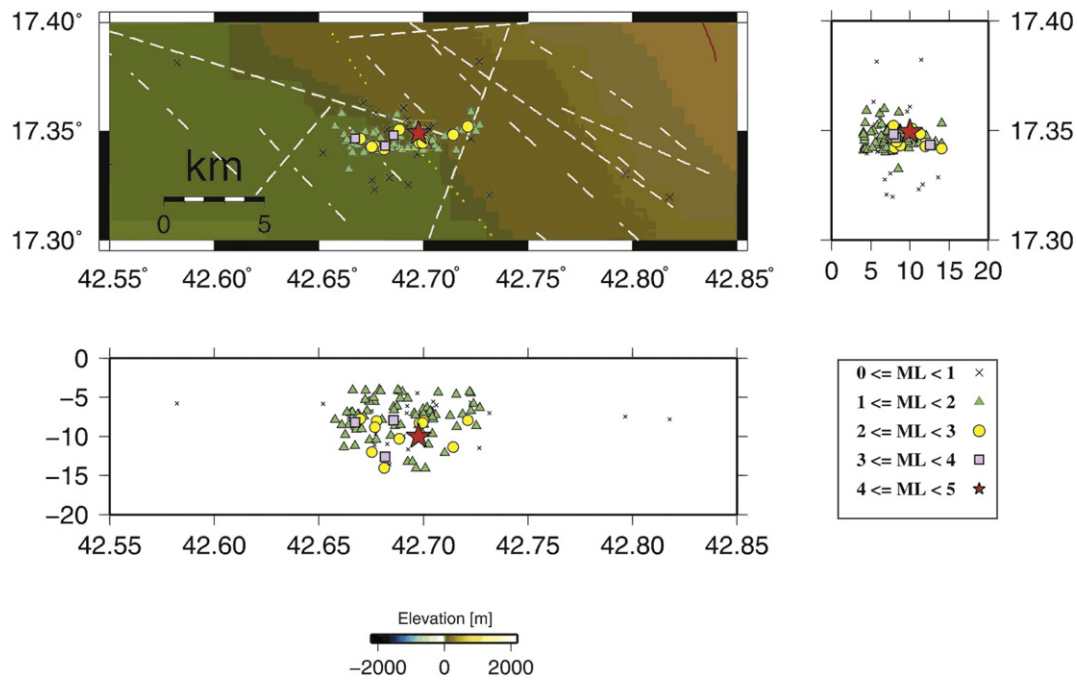


**Fig. 3.** The distribution of epicenters, the red star refers to the mainshock and the rectangle represents the seismic dislocation area. The right panel is the distribution of hypocenters along the latitude and the bottom panel is the distribution of hypocenters along the longitude. Different symbols correspond to magnitude classification. Yellow dot and white dashed lines represent the fault traces inferred from gravity and magnetic data, respectively. (For interpretation of the references to colour in this figure legend, the reader is referred to the web version of this article.)

shape ratio using the linear inversion technique proposed by Michael (1984) to identify the fault plane. Using a grid search method, the iterative procedure was repeated over the friction coefficients in the range of 0.2–1.0.

The focal mechanism solutions of total number of 15 events were used to invert the stress tensor. Fig. 6 displays the stress tensor inversion results for the friction coefficient of 0.40 and the shape ratio of 0.52 that retrieved from the grid search algorithm. The principal stress axes of the best fitting model for the focal mechanism dataset showed that the maximum compressive stress,  $\sigma_1$ , has a nearly horizontal plunge of  $12.8^\circ$  toward ESE and that the minimum compressive stress,  $\sigma_3$ , has a shallow horizontal plunge of  $0.3^\circ$  toward NNE; corresponding to the dominant strike-slip stress regime as illustrated in Fig. 6a. The principal compressive stress axes  $\sigma_1$ ,  $\sigma_2$  and  $\sigma_3$  (the maximum, intermediate and minimum) are listed in Table 3. Owing to this stress regime, the compatible focal mechanisms reflected strike-slip faulting with fault plane dipping at a nearly vertical angle. As shown in Fig. 6b, the fault plane solutions identified by the stress inversion are clustered in the validity area of Mohr–Coulomb failure criterion; reflecting the consistency of the data with the fault instability model (Vavryčuk, 2014). The causative fault was resolved with strike of  $260.5^\circ$ , dip of  $83.6^\circ$ , and rake of  $-170^\circ$ . Estimates of the uncertainty in stress axes, as provided by the STRESSINVERSE code, are shown in Fig. 6c. The figure showed high confidence level to determine the best stress directions of  $\sigma_1$ ,  $\sigma_2$  and  $\sigma_3$ ; interpreted as shear stress regime of a slight dip-slip displacement.

## 5. Coulomb stress

The stress regime, controlling the spatial distribution of foreshocks and aftershocks, is investigated using the distribution of Coulomb stress changes. The software used in this analysis was the Coulomb software, version 3.3 (Toda et al., 1998). The software uses the analytical formulae of Okada (1992) and boundary element formulae (Crouch and Starfield, 1983). In Okada (1992), dislocations are on rectangular planes embedded in a homogeneous and isotropic half-space (King et al., 1994; Stein et al., 1994). The static stress changes are expressed as changes in the

Coulomb failure function,  $\Delta$  CFF, which is the sum of the shear stress change in the direction of fault slip, the change in normal stress and the change in pore pressure. This last parameter approximated the volumetric stress change, assuming that fault zone materials are more ductile than the surrounding rocks (Rice, 1992; Harris, 1998).

The Coulomb stress pattern was computed for the mainshock of Mw 4.4 and focal mechanism of a dextral lateral strike-slip fault plane with strike of  $260.5^\circ$ , dip of  $83.6^\circ$  and rake of  $-170^\circ$ , as obtained from the stress tensor inversion. The friction coefficient was assigned a value of 0.4, as determined from the stress tensor inversion. Estimates of stress transfer were done by assuming an elastic half-space with a shear modulus,  $\mu$ , of 30 GPa and a Poisson's ratio of 0.25. A reasonable fault dimension can be estimated by assuming a circular crack with constant stress drop of 3 MPa and using the given Mw 4.4, the fault area is about  $3 \text{ km}^2$ , or has a radius of about 1 km; yielding a slip value of 0.06 m. Alternately, the spatial extension of the aftershocks during the first 24 h was used as a proxy to estimate the rupture area of 1.8 km length and 1.5 km width; giving a slip value (D) of 0.06 m as derived from the relationship between the seismic moment (Mo), rigidity ( $\mu$ ) and the fault area (A);  $M_o = \mu \cdot A \cdot D$ . By assuming a rectangular fault of reasonable dimension (1.8 km length and 1.5 km width) and then considering a uniform slip of 0.06 m, the distribution of  $\Delta$ CFS pattern, triggered from the mainshock, was computed as shown in Fig. 7. The figure shows a good correlation between the positive  $\Delta$ CFS pattern and the aftershock distributions.

## 6. Discussions

In this study, our results showed a good correlation between aftershock distribution, focal mechanism solutions, stress tensor inversion and the distribution of Coulomb stress changes along the active fault of dextral strike-slip displacement. The results suggested that the 2014 Jizan earthquake sequence slipped over a high-angle fault buried in Precambrian basement of dextral strike-slip displacement along the ENE trend.

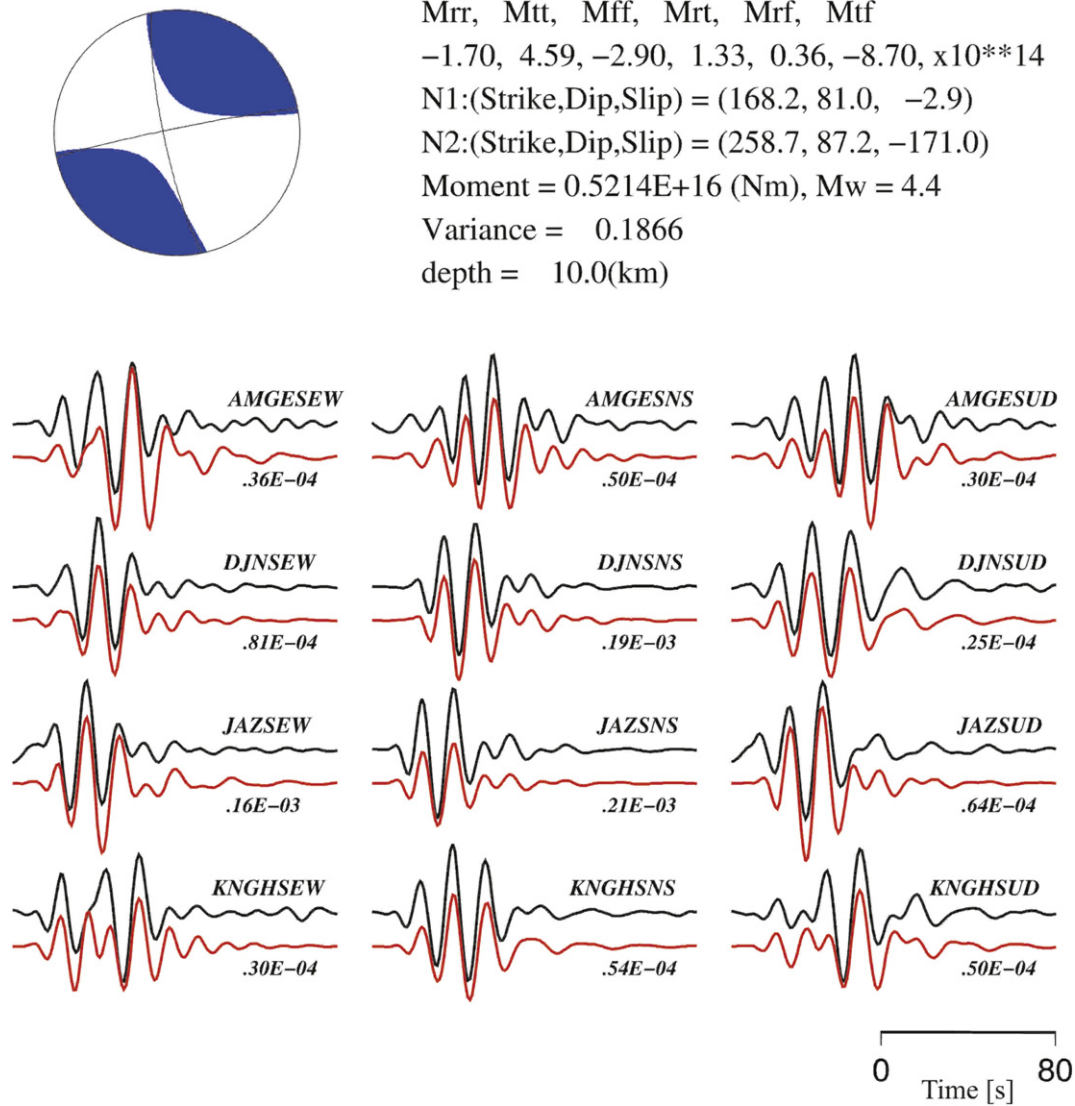


**Fig. 4.** Comparison between observed (black lines) and synthetic (red lines) waveforms obtained from the focal mechanism solution (beach-ball) as deduced from moment tensor inversion for the mainshock that occurred on the 23th of January 2014 at 15:00:37 (UTC). Synthetic and observed waveforms were filtered between 0.01 and 0.1 Hz. Station code and maximum amplitude in cm are indicated on the right of each set of traces, respectively. (For interpretation of the references to colour in this figure legend, the reader is referred to the web version of this article.)

Among the 2014 Jizan earthquake sequence, the epicentres distribution demarcated a fault elongated along the ENE-WSW trend; reflecting a seismic dislocation area of approximately 6 km fault length and 2 km width (Fig. 3). The vertical sections parallel to the latitude and longitude revealed that aftershock hypocenters were distributed downward and upward from the mainshock hypocenter. A total number of four focal mechanisms for the events of magnitude larger than 3.5 were retrieved using the moment tensor inversion technique. The modelling of amplitude spectrum constraint with the first motion polarities of P waves (eleven earthquakes) were used to determine focal mechanisms for eleven aftershocks in the magnitude range of 2–3. The focal mechanisms showed two distinct nodal planes; the first one is oriented in the ENE-WSW direction and the second one has a strike of NNW-SSE (Fig. 5). The ENE-WSW nodal plane supports the aftershock distribution; reflecting a dextral strike-slip with dip-slip displacement. The stress tensor inversion, as shown in Fig. 6, implied that the maximum compressive stress,  $\sigma_1$ , is WNW-ESE oriented with a nearly shallow plunge of  $11.8^\circ$  while the minimum compressive stress,  $\sigma_3$ , is NNE-SSW oriented with a horizontal plunge of  $0.3^\circ$ . Owing to the given stress domain, the stress tensor inversion identified the ENE fault as the fault plane. This result indicates that the epicentral area is currently influenced by seismic

deformation due to the WNW-ESE compressive and NNE-SSW extensive stress regime. To this end, a good correlation was observed between the aftershock distributions and the positive region of Coulomb stress distributions (Fig. 7); suggesting that the mainshock rupture controlled the aftershocks activity.

The Centroid Moment Tensor (CMT) solutions for larger earthquakes along the plate boundaries in the Red Sea, Gulf of Aqaba, Dead Sea fault system, and the Gulf of Aden showed normal to strike-slip faulting of dominant extensional to shear stress regime over the region. Considering fault systems in the Arabian Shield, two fault sets are recognized in the Arabian Shield (Hansen et al., 2013). The first trend is considered as the active fault of extensional field in the Shield that parallels to the Red Sea spreading axis of NW-SE strike. The second trend represents dextral strike-slip displacement along the NE-SW to ENE-WSW trending system that originated with the oldest Precambrian Orogeny (Beydoun et al., 1998). The geophysical seismic surveys of Chandrasekharam et al. (2015) depicted the ENE fault trend in Jizan area. The earthquakes that occurred recently in the northwestern Saudi Arabia exhibited dip-slips along normal faults oriented parallel to the Red Sea. Accordingly, the NNW plane of strike-slip or dip-slip displacements can be selected as the preferred fault that produced the 23rd January earthquake sequences.

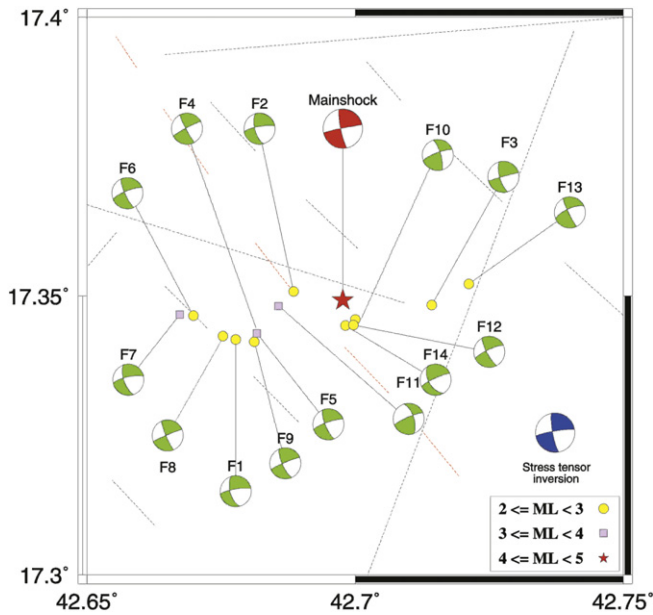


**Fig. 5.** The distribution of focal mechanisms of the mainshock and fourteen aftershocks of  $M_L > 2.0$ , identified as F1 to F14 as listed in Table 2. The red star refers to the epicentre of the mainshock. Different symbols corresponded to magnitude classification as shown in the legend. Red and black dashed lines represent the fault traces inferred from gravity and magnetic data, respectively. (For interpretation of the references to colour in this figure legend, the reader is referred to the web version of this article.)

However, accurate relocations and focal mechanism solutions presented in this study suggest another scenario. The coincidence of the epicentre distributions and one of the nodal planes, as obtained from focal mechanism analysis, indicated that the ENE–WSW fault trend is the likely causative fault. Tectonically, three rifting plate boundaries, the Red Sea, the Gulf of Aden, and the East African Rift control the seismic activity in the region. The appearance of strike-slip faulting mechanisms in the Red Sea and Gulf of Aden is tectonically consistent with the tectonic processes associated with the anticlockwise rotation of Arabian Shield due to the rifting in Red Sea and Gulf of Aden; reflecting that strike-slip faulting modes are expectable. Moreover, sinistral and dextral strike-slip faults are widely distributed in the region. For instance, the major sinistral strike-slip displacements are recognized by the shear stress regime in the Gulf of Aqaba, Dead Sea transform fault zone and East Anatolian fault. On the other hand, the dextral strike-slip displacements are consistent with the shear movements along the Owen fracture zone, North Anatolian fault, Oman line and the Hadibo transfer zone in Yemen. The dextral strike-slip faults represented reactivated Precambrian Pan-African structures (Greenwood et al., 1980). It is noteworthy that there are numerous Red-Sea parallel structures that sometimes are referred

**Table 3**  
Principal stress axes and the optimum fault trends.

Stress axis	Azimuth [°]	Plunge [°]	
$\sigma_1$	114.1	11.8	
$\sigma_2$	292.7	78.2	
$\sigma_3$	24.0	0.3	
Optimum fault trends	Strike [°]	Dip [°]	Rake [°]
Lower Mohr's semi-circle	260.5	83.6	–170.0
Upper Mohr's semi-circle	147.5	83.2	–9.7

to as Cenozoic faults. It is obvious that the respective event is not related to one of these faults.

However, faults inferred from gravity and magnetic data (Gettings, 1983) provide evidence of ENE-striking structure emanating from the Red-Sea rifting and may form some delineations that are in consistence with the strike of this event; indicating the reactivation of a buried fault in the Precambrian basement that is compatible with the ambient stress domain in the region.

## 7. Conclusions

Based on the detailed analysis presented through precise earthquake locations, focal mechanism solutions, stress tensor inversion, and Coulomb failure stress, we mapped the causative fault of the 2014 earthquake sequence, Jizan area, Saudi Arabia. The aftershock distributions delineated a fault plane of ENE–WSW trend that is almost conjugate to the Red Sea spreading axis and NNW–SSE NFS. This fault trend is the consistent one of two nodal planes obtained from focal mechanism solutions determined by moment tensor inversion and waveform modelling. The stress tensor inversion identified the active fault delineated by the aftershock distributions and focal mechanism solutions. The analysis of  $\Delta CFS$  emphasized the active fault striking ENE–WSW. The active fault mapped in this study indicates reactivation of a pre-existing fault buried in Precambrian basement due to the contemporary stress regime of a nearly horizontal compressive stress,  $\sigma_1$ , approximately 11.8° plunge trending ESE and a horizontal compressive stress,  $\sigma_3$ , of 0.3° plunge striking NNE; obtaining a dextral strike-slip fault strikes combined with a dip-slip of normal displacement. The optimum fault plane solution reflects focal parameters of N260.5°E strike, dipping with a steep angle of 83.6° to the north, and slipping with an angle of –170°.

## Acknowledgments

We are grateful to the Saudi Geological Survey (SGS) for providing the broadband seismic data. The authors would like to extend their sincere appreciation to the Deanship of Scientific Research at King Saud University for funding this Research group no. (RG-1437-010). Authors

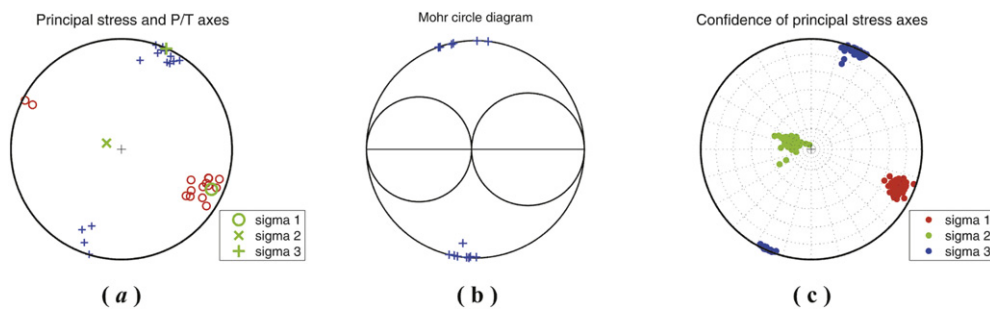


**Fig. 6.** Stress inversion based on fifteen focal mechanism solutions. (a) P (red) & T (blue) axes and the stress directions  $\sigma_1$ ,  $\sigma_2$  and  $\sigma_3$ . (b) Mohr's circle with the identified faults shown by blue crosses. (c) Relative uncertainty of the stress axes resulting from random perturbation of the input data. (For interpretation of the references to colour in this figure legend, the reader is referred to the web version of this article.)

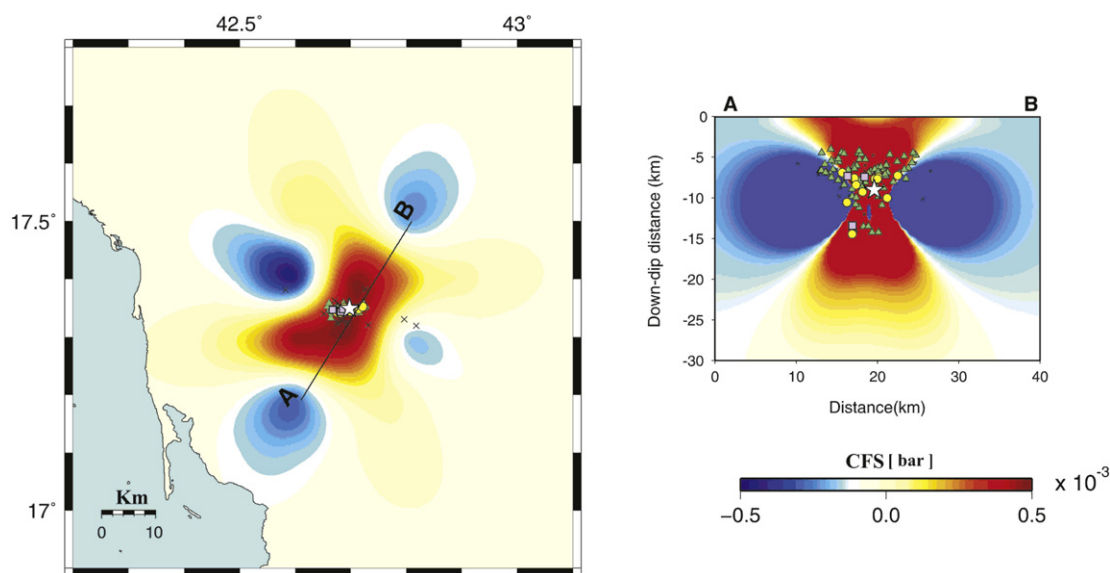


**Fig. 7.** Map showing the distribution of Coulomb stress changes using the fault parameters, listed in Table 3, as retrieved from the stress tensor inversion. (a) the Coulomb stress changes at a depth of 10 km caused by the mainshock of the 2014 Jizan earthquake and (b) cross section of Coulomb stress changes along the profile AB. The white star refers to the mainshock and aftershocks are represented by similar symbols as displayed in Fig. 3.

would like to thank Martin Mai and an anonymous reviewer for their critical reviews and comments for improving the manuscript. The Coulomb failure was calculated using the package Coulomb3.4. Generic Mapping Tools developed by Wessel and Smith (1998) was used for data mapping.

## References

- Abdel-Fattah, A.K., Al-Amri, A.M., Fnais, M.S., Abdelrahman, K., 2014. Estimation of source parameters and attenuation using digital waveforms of Al-Ays 2009 earthquake, Saudi Arabia. *Arab. J. Geosci.* 7, 3325–3337.
- Agar, R.A., 1992. The tectono-metallogenic evolution of the Arabian shield. *Precambrian Res.* 58, 169–194.
- Aldamegh, K., Abou Elenean, K., Hussein, H., Rodgers, A., 2009. Earthquake sequence, eastern Red Sea margin, Kingdom of Saudi Arabia. *J. Seismol.* <http://dx.doi.org/10.1007/s10950-008-9148-5>.
- Aldamegh, K., Hussein, H., Al-Arifi, N., Moustafa, S., Moustafa, M., 2012. Focal mechanism of Badr earthquake, Saudi Arabia of August 27, 2009. *Arab. J. Geosci.* 5, 599–606.
- ArRajehi, A., McClusky, S., Reilinger, R., Daoud, M., Alchalbi, A., Ergintav, S., Gomez, F., Sholan, J., Bou-Rabee, F., Ogubazghi, G., Haileab, B., 2010. Geodetic constraints on present-day motion of the Arabian plate: implications for Red Sea and Gulf of Aden rifting. *Tectonics* 29 (3).
- Augustin, N., van der Zwan, F.M., Devey, C.W., Ligi, M., Kwasnitschka, T., Feldens, P., Bantan, R.A., Basaham, A.S., 2016. Geomorphology of the central Red Sea rift: determining spreading processes. *Geomorphology* 274, 162–179.
- Beydoun, Z.R., As-Saruri, M.L., El-Nakhal, H., Al-Ganad, I.N., Baraba, R.S., Nani, A.O., Al-Aawah, M.H., 1998. International Lexicon of Stratigraphy, Republic of Yemen. VIII, Asia, fasc. 10b2. 34. IUGS Publ., pp. 1–245.
- Bonatti, E., 1985. Punctiform initiation of seafloor spreading in the Red Sea during transition from a continental to an oceanic rift. *Nature* 316, 33–37.
- Bouchon, M., 1981. A simple method to calculate Green's functions for elastic layered media. *Bull. Seismol. Soc. Am.* 71, 959–971.
- Camp, V.E., Roobol, M.J., 1989. The Arabian continental alkali basalt province: part I, evolution of Harrat Rahat, Kingdom of Saudi Arabia. *Geol. Soc. Am. Bull.* 101, 71–95.
- Carbotte, S.M., Smith, D.K., Cannat, M., Klein, E.M., 2015. Tectonic and magmatic segmentation of the Global Ocean Ridge System: a synthesis of observations. In: Wright, T.J., Ayele, A., Ferguson, D.J., Kidane, T., Vye-Brown, C. (Eds.), *Magmatic Rifting and Active Volcanism*. *Geol. Soc. Spec. Pub.* Vol. 420, pp. 1–47.
- Chandrasekharan, D., Lashin, A., Al Arifi, N., Al Bassam, A., Ranjith, P.G., Varun, C., Singh, H.K., 2015. Geothermal energy resources of Jizan, SW Saudi Arabia. *JAES* 109, 55–67.
- Chu, D., Gordon, R., 1998. Current plate motions across the Red Sea. *Geophys. J. Int.* 135, 313–328.
- Coleman, R.G., 1977. Geological background of the Red Sea. In: Hilpert, L.S. (Ed.), *Red Sea Research 1970–1975*. Saudi Arabian Dir. Gen. Mineral Resources Bull., pp. C1–C9.
- Coleman, R.G., Fleck, R.J., Hedge, C.E., Ghent, E.D., 1977. The volcanic rocks of southwest Saudi Arabia and the opening of the Red Sea. *Mineral Resources Bull.* 22D. Red Sea Research, Jeddah, Saudi Arabia, pp. D1–D30.
- Coutant, O., 1989. Program of Numerical Simulation AXITRA. Research Report. LGIT, Grenoble.
- Craig, T.J., Jackson, J.A., Priestley, K., McKenzie, D., 2011. Earthquake distribution patterns in Africa: their relationship to variations in lithospheric and geological structure, and their rheological implications. *GJI* 185, 403–434.
- Crouch, S.L., Starfield, A.M., 1983. *Boundary Element Methods in Solid Mechanics*. Allen Unwin, London (322 pp.).
- Dick, H.J.B., Lin, J., Schouten, H., 2003. An ultraslow-spreading class of ocean ridge. *Nature* 426:405–412. <http://dx.doi.org/10.1038/nature02128>.
- El-Hadidy, S., 2015. Seismicity and seismotectonic setting of the Red Sea and adjacent areas. In: Rasual, N.M.A., Stewart, I.C.F. (Eds.), *The Red Sea: The Formation, Morphology, Oceanography and Environment of a Young Ocean Basin*. Springer, London, pp. 151–159.
- Fournier, M., Huchon, P., Khanbari, K., Leroy, S., 2007. Asymmetry and segmentation of passive margin in Socotra, Eastern Gulf of Aden, controlled by detachment faults? *Geochem. Geophys. Geosyst.* 8 (3), Q03013 (03010.01029/02006G001318).
- Gettings, M.E., 1983. A simple Bouguer gravity anomaly map of southwestern Saudi Arabia and an initial interpretation. Open File Rep. USGS-OF-03-94. U.S. Geol. Surv. Saudi Arabia Mission. Saudi Arabia Deputy Minist. for Miner. Resour., Jeddah (89 pp.).
- Girdler, M.E., Underwood, M., 1985. The evolution of early oceanic lithosphere in the northern Red Sea. *Tectonophysics* 116, 95–108.
- Greenwood, W.R., Anderson, R.E., Fleck, R.J., Roberts, R.J., 1980. Precambrian geology history and plate tectonic evolution of the Arabian shield. *Saudi Arabia Directorate General of Mineral Resources Bulletin.* 24, pp. 1–35.
- Hanks, T.C., Kanamori, H., 1979. A moment magnitude scale. *JGR* 84, 2348–2350.
- Hansen, S.E., DeShon, H.R., Moore-Driskell, M.M., Al-Amri, A., 2013. Investigating the P wave velocity structure beneath Harrat Lunayyir, northwestern Saudi Arabia, using double-difference tomography and earthquakes from the 2009 seismic swarm. *JGR* 118, 4814–4826.
- Harris, R.A., 1998. Introduction to special section: stress triggers, stress shadows, and implications for seismic hazard. *J. Geophys. Res.* 103, 24347–24358.
- Herrmann, R.B., Ammon, C.J., 2004. Computer programs in seismology. *Manual of the Generic Seismic Application Coding (GSAC)*. Saint Louis University (Version 3.30).
- Husseini, M.I., 1988. The Arabian Infracambrian extension system. *Tectonophysics* 148 (93), 103.
- Jansky, J., 2001. Ray-method Calculations of the Travel Times and Take-off Angles in Gradient Models, Program ANGGRA, Research Report. Dept. of Geophysics, Faculty of Math. and Phys., Charles University, Prague.
- Johnson, P.R., 1998. Tectonic Map of Saudi Arabia and Adjacent Areas. Deputy Ministry for Mineral Resources, Saudi Arabia (USGS TR-98-3).
- King, G.C.P., Stein, R.S., Lin, J., 1994. Static stress changes and the triggering of earthquakes. *Bull. Seismol. Soc. Am.* 84, 935–953.
- Kohketsu, K., 1985. The extended reflectivity method for synthetic near-field seismograms. *J. Phys. Earth* 33, 121–131.
- Mancilla, P., 2001. Surface Wave Dispersion About the New Madrid Region. (MSc thesis). Faculty of the Graduate School of Saint Louis University, USA.
- McClusky, S., Reilinger, R., Ogubazghi, G., Amleson, A., Healeb, B., Vernant, Ph., Sholan, J., Fisseha, Sh., Asfaw, L., Bendick, R., Kogan, L., 2010. Kinematics of the southern Red Sea-Afar Triple Junction and implications for plate dynamics. *GRL* 37, L05301.
- Michael, A.J., 1984. Determination of stress from slip data: faults and folds. *J. Geophys. Res.* Solid Earth 89 (B13), 11517–11526.
- Okada, Y., 1992. Internal deformation due to shear and tensile faults in a half-space. *Bull. Seismol. Soc. Am.* 82 (2), 1018–1040.
- Plicka, V., Zahradnik, J., 2014. Inverting full waveforms into 1D seismic velocity model of the upper crust by neighbourhood algorithm-Gorinth Gulf, Greece. *Stud. Geophys. Geod.* 58, 388–402.
- Rasul, N.M., Stewart, I.C., Nawab, Z.A., 2015. Introduction to the Red Sea: its origin, structure, and environment. *The Red Sea*. Springer, Berlin Heidelberg, pp. 1–28.
- Reilinger, R., McClusky, S., Vernant, P., Lawrence, S., Ergintav, S., Cakmak, R., Ozener, H., Kadirov, F., Guliev, I., Stepanyan, R., Nadariya, M., 2006. GPS constraints on continental

- deformation in the Africa-Arabia-Eurasia continental collision zone and implications for the dynamics of plate interactions. *J. Geophys. Res. Solid Earth* 111 (B5).
- Rice, J., 1992. Fault stress states, pore pressure distributions and the weakness of the San Andreas fault. In: Evans, B., Wong, T.-F. (Eds.), *Fault Mechanics and Transport Properties of Rock*. Academic, San Diego, Calif., pp. 475–503.
- Ritsema, J., Lay, T., 1995. Long period regional waves moment tensor inversion for earthquakes in the western United States. *JGR* 100, 9853–9864.
- Rodgers, A., Walter, W., Mellors, R., Al-Amri, A., Zhang, Y., 1999. Lithospheric structure of the Arabian shield and platform from complete regional waveform modelling and surface wave group velocities. *GJI* 138, 871–878.
- Stein, R.S., King, G.C.P., Lin, J., 1994. Stress triggering of the 1994  $M = 6.7$  Northridge, California, earthquake by its predecessors. *Science* 265, 1432–1435.
- Stern, R.J., Johnson, P., 2010. Continental lithosphere of the Arabian plate: a geologic, petrologic, and geophysical synthesis. *Earth Sci. Rev.* 101, 29–67.
- Toda, S., Stein, R.S., Reasenber, P.A., Dieterich, J.H., 1998. Stress transferred by the  $M_w = 6.5$  Kobe, Japan, shock: effect on aftershocks and future earthquake probabilities. *J. Geophys. Res.* 103, 24,543–24,565.
- Vavryčuk, V., 2014. Iterative joint inversion for stress and fault orientations from focal mechanisms. *GJI* 199 (1), 69–77.
- Vavryčuk, V., 2015. Moment tensor decompositions revisited. *J. Seismol.* 19 (1), 231–252.
- Vita-Finzi, C., 2001. Neotectonics at the Arabian plate margins. *J. Struct. Geol.* 23, 521–530.
- Wessel, P., Smith, W.H., 1998. New, improved version of Generic Mapping Tools released. *EOS Trans. Am. Geophys. Union* 79 579–579.
- Yagi, Y., Nishimura, N., 2011. Moment tensor inversion of near-source seismograms. *Bull. IISSE* 45, 133–138.
- Zahradnik, J., Janski, J., Papatsimpa, K., 2001. Focal mechanisms of weak earthquakes from amplitude spectra and polarities. *Pure Appl. Geophys.* 158, 647–665.